Modeling lidar waveforms with time-dependent stochastic radiative transfer theory for remote estimations of forest structure

Svetlana Y. Kotchenova,[1] Nikolay V. Shabanov,[1] Yuri Knyazikhin,[1] Anthony B. Davis,[2] Ralph Dubayah,[3] and Ranga B. Myneni[1]

Received 4 December 2002; revised 14 March 2003; accepted 27 March 2003; published 15 August 2003.

[1] Large footprint waveform-recording laser altimeters (lidars) have demonstrated a potential for accurate remote sensing of forest biomass and structure, important for regional and global climate studies. Currently, radiative transfer analyses of lidar data are based on the simplifying assumption that only single scattering contributes to the return signal, which may lead to errors in the modeling of the lower portions of recorded waveforms in the near-infrared spectrum. In this study we apply time-dependent stochastic radiative transfer (RT) theory to model the propagation of lidar pulses through forest canopies. A time-dependent stochastic RT equation is formulated and solved numerically. Such an approach describes multiple scattering events, allows for realistic representation of forest structure including foliage clumping and gaps, simulates off-nadir and multiangular observations, and has the potential to provide better approximations of return waveforms. The model was tested with field data from two conifer forest stands (southern old jack pine and southern old black spruce) in central Canada and two closed canopy deciduous forest stands (with overstory dominated by tulip poplar) in eastern Maryland. Model-simulated signals were compared with waveforms recorded by the Scanning Lidar Imager of Canopies by Echo Recovery (SLICER) over these regions. Model simulations show good agreement with SLICER signals having a slow decay of the waveform. The analysis of the effects of multiple scattering shows that multiply scattered photons magnify the amplitude of the reflected signal, especially that originating from the lower portions of the canopy. *INDEX TERMS:* 1640 Global Change: Remote sensing; 1694 Global Change: Instruments and techniques; 1699 Global Change: General or miscellaneous; *KEYWORDS:* remote sensing of vegetation canopies, time-dependent radiative transfer model, lidar waveforms, multiple scattering

Citation: Kotchenova, S. Y., N. V. Shabanov, Y. Knyazikhin, A. B. Davis, R. Dubayah, and R. B. Myneni, Modeling lidar waveforms with time-dependent stochastic radiative transfer theory for remote estimations of forest structure, *J. Geophys. Res.*, *108*(D15), 4484, doi:10.1029/2002JD003288, 2003.

1. Introduction

[2] Monitoring and modeling three-dimensional forest structure has long been one of the main tasks for many of the space missions [e.g., *Ranson et al.*, 1997; *Castel et al.*, 2001]. Forests play an important role in the exchange of heat, momentum and carbon between the land surface and the atmosphere. The rate of exchange mostly depends on the horizontal and vertical distribution of canopy material. Ground measurements of this distribution are expensive, limited to small areas, time consuming, and difficult to repeat. Remote sensing technology has the advantages of high spatial resolution, temporal consistency, mapping large areas and quantifiable uncertainty.

[3] A new class of instruments, large footprint waveform-recording laser altimeters (lidars), has demonstrated a potential to significantly improve remote estimates of vertical forest structure. The group includes the previously used Scanning Lidar Imager of Canopies by Echo Recovery (SLICER), the current airborne Laser Vegetation Imaging Sensor (LVIS), and possibly the spaceborne Vegetation Canopy Lidar (VCL). The lasers have large footprints (10–15 m in diameter for SLICER and 25 m for VCL and LVIS) and operate in the near infrared (NIR) spectrum at 1064 nm. The data collected by SLICER and LVIS confirm the potential of large footprint lidar instruments to recover forest structural attributes [*Drake et al.*, 2002; *Lefsky et al.*, 2002; *Lefsky et al.*, 1999a, 1999b; *Means et al.*, 1999].

[4] Instruments such as VCL provide information about canopy height and vertical distribution of nadir intercepted surfaces [*Dubayah et al.*, 1997, 2000]. A laser altimeter waveform is a record of the amplitude of backscattered laser energy from the Earth's surface (in the absence of clouds) as

[1]Department of Geography, Boston University, Boston, Massachusetts, USA.
[2]Space and Remote Sensing Sciences Group, Los Alamos National Laboratory, Los Alamos, New Mexico, USA.
[3]Department of Geography, University of Maryland, College Park, Maryland, USA.

Copyright 2003 by the American Geophysical Union.
0148-0227/03/2002JD003288$09.00

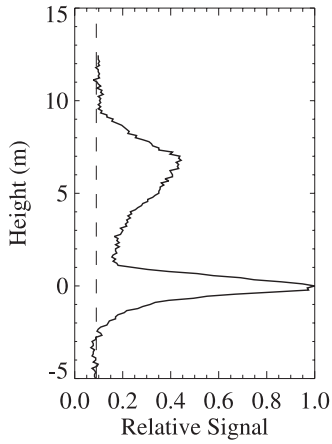

Figure 1. Waveform profile measured with the SLICER instrument over an old black spruce forest in the BOREAS Southern Study Area. The waveform is normalized by the maximum return. The noise level is shown as a dashed line.

a function of time. Both single and multiple scattering events contribute to the return signal. Travel time is converted to distance based on the speed of light in the atmosphere (Figure 1). The first significant return above a noise threshold is used to estimate the top of the canopy, the midpoint of the last return represents the reflection from the ground, and canopy height is calculated as the distance between these two returns. The amplitude of the recorded waveform measures the strength of the return. For surfaces with similar reflective properties and geometry within a footprint (and under similar atmospheric conditions), the larger amplitude indicates more canopy material.

[5] The development of large footprint lidars has raised questions related to effects of multiple scattering, reliability of detecting canopy closure, and analysis of the signal for retrieval of tree structural parameters. There are various types of retrievals of forest structure from lidar [*Dubayah et al.*, 2000]. Some structure is directly measured, such as canopy height and subcanopy topography. Other structure must be modeled or inferred, most notably biomass. While lidar provides a direct record of the vertical distribution of nadir-intercepted surfaces, the subsequent interpretation of this record in terms of the canopy material, or as vertical foliar diversity, requires knowledge and modeling of the relationships between lidar waveforms and the spatial structure and optical properties of the vegetation. For example, there are well documented shadowing effects as upper surfaces obscure those lower in the canopy and extinction coefficients have been used to adjust for this effect under simplifying assumptions, such as uniform horizontal leaf distributions [e.g., see *Drake et al.*, 2002; *Harding et al.*, 2001]. A number of computer-based models, which simulate the interaction between stand elements and lidar pulses, have been developed to more fully investigate these relationships [e.g., *Sun and Ranson*, 2000; *Ni-Meister et al.*, 2001]. These models are based on the assumption that only single scattering contributes to the return signal, which may lead to errors in the modeling of the lower portions of recorded waveforms in the near-infrared spectrum.

[6] A pulse emitted in the visible spectral region is strongly absorbed by the vegetation, and the reflected signal results almost exclusively from single scattering. On the other hand, in the NIR spectral region, a pulse is weakly absorbed and penetrates deeper into the canopy and the returned waveform is significantly affected by multiple scattering, especially in the case of dense forests [*Govaerts*, 1996]. Ray tracing models have been used to simulate high-order scattering but they require knowledge of the tree height, crown shape, and foliage density, which is difficult to obtain in practice. The effects of multiple scattering are mainly exhibited in a shift in the observed waveforms. The path for multiply scattered photons is longer than the straight line path between the instrument and the target, and thus those photons appear delayed in the waveform [*Harding et al.*, 2001]. The higher the density, the longer the path photons travel before exiting the canopy. Inclusion of multiple scattering events possibly results in a more accurate approximation of the recorded waveform. Given a good waveform approximation, some tree structural parameters, such as vertical foliage diversity, may be retrieved with higher accuracy.

[7] In cloud remote sensing, the behavior of multiply scattered photons is described with a stochastic time-independent radiative transfer equation [e.g., *Titov*, 1990; *Malvagi et al.*, 1993]. Equations for the mean intensity of radiation field are derived and solved numerically using the Monte Carlo or SOSA (successive orders of scattering approximations) methods. Such an approach was first applied to vegetation by *Shabanov et al.* [2000] to simulate a stable radiation regime in discontinuous canopies. The quality of simulations was assessed by comparison with field data from shrub lands. Good agreement was obtained between modeled and field-measured values of transmitted and absorbed radiation.

[8] This paper will demonstrate the application of time-dependent stochastic radiative transfer theory for modeling the propagation of lidar signals through vegetation canopies. Such an approach includes multiple scattering events, allows for realistic representation of forest structure including clumping and gaps, simulates off-nadir and multiangular observations, and has the potential to provide better approximations of real recorded waveforms. The model simulations will be compared with the SLICER return signals for four different forest stands. Finally, we offer an algorithm for the estimation of photon mean free path and extinction coefficient from the difference between waveforms originating from single and multiple scattering. We followed the ideas developed in cloud remote sensing where the account for multiple scattering events allows accurate retrievals of physical and optical cloud thicknesses [*Davis et al.*, 1999], especially using space-borne lidar [*Davis et al.*, 2001].

2. Background Theory

[9] Consider a vegetation canopy located within the layer $0 < z < H$. The top ($z = 0$) and bottom ($z = H$) surfaces form its upper and lower boundaries. A lidar beam illuminates a vertical vegetation stand of the diameter of the laser footprint. Because of the small divergence angle, photons can be assumed incident parallel on the top of the stand. The transmitted energy decreases with depth because of reflection and absorption by leaves, twigs, branches, and trunks,

at various heights. The radiation regime inside the canopy is strongly time-dependent because of the short duration of a lidar pulse.

[10] The propagation of photons through vegetation is described by the time-dependent three-dimensional (3D) radiative transfer equation

$$\frac{1}{c}\frac{\partial I_\lambda\left(t,\vec{r},\vec{\Omega}\right)}{\partial t}+\vec{\Omega}\bullet\nabla I_\lambda\left(t,\vec{r},\vec{\Omega}\right)+\chi(\vec{r})\cdot\sigma\left(\vec{\Omega}\right)\cdot I_\lambda\left(t,\vec{r},\vec{\Omega}\right)=\chi(\vec{r})\cdot\int\limits_{4\pi}\sigma_S\left(\vec{\Omega}'\rightarrow\vec{\Omega}\right)\cdot I_\lambda\left(t,\vec{r},\vec{\Omega}'\right)d\vec{\Omega}', \quad (1)$$

where $I_\lambda(t,\vec{r},\vec{\Omega})$ is the intensity of radiation at point $\vec{r}$ in direction $\vec{\Omega}$ at time t; λ is a wavelength at which the lidar operates; $\vec{\Omega}\bullet\nabla$ is a derivative at $\vec{r}$ along direction $\vec{\Omega}$; and

$$\chi(\vec{r})=\begin{cases}1, & \text{if there is a leaf at } \vec{r},\\ 0, & \text{otherwise,}\end{cases} \quad (2)$$

is an indicator function describing the canopy structure; $\sigma(\vec{\Omega})$ is the extinction coefficient, and $\sigma_s(\vec{\Omega}'\rightarrow\vec{\Omega})$ is the differential scattering coefficient.

[11] The indicator function is treated as a random variable. The solution of equation (1) therefore is also a random variable. It depends on both macroscale (e.g., random dimensions of the trees and their spatial distribution) and microscale (e.g., structural organization of an individual tree) properties of vegetation [*Knyazikhin et al.*, 1998]. The presence of $\chi(\vec{r})$ allows us to refer to equation (1) as "stochastic".

[12] In the classical RTE, the extinction and differential scattering coefficients are defined as $\sigma(\vec{r},\vec{\Omega})=u_L(\vec{r})G(\vec{r},\vec{\Omega})$ and $\sigma_S(\vec{r},\vec{\Omega}'\rightarrow\vec{\Omega})=\frac{u_L(\vec{r})}{\pi}\Gamma(\vec{r},\vec{\Omega}'\rightarrow\vec{\Omega})$, where $u_L(\vec{r})$ is the leaf area volume density; $G(\vec{r},\vec{\Omega})$ is the Ross-Nilson G function; and $\Gamma(\vec{r},\vec{\Omega}'\rightarrow\vec{\Omega})$ is the area scattering phase function. Detailed descriptions of these variables are given by *Ross* [1981], *Myneni* [1991], and *Shultis and Myneni* [1988]. Below, the formulation of *Myneni* [1991] is adopted. We assume that the G function and the area scattering phase function do not depend on the spatial variable $\vec{r}$. We introduce the mean leaf area volume density of a foliated point as

$$u_L=\frac{\int\limits_{0<z<H}u_L(\vec{r})d\vec{r}}{\int\limits_{0<z<H}\chi(\vec{r})d\vec{r}}. \quad (3)$$

[13] The distribution of foliated points is given by the indicator function (see equation (2)). The extinction and differential scattering coefficients appearing in the time-dependent stochastic transport equation (1) are $\chi(\vec{r})\sigma(\vec{\Omega})$ and $\chi(\vec{r})\sigma_S(\vec{\Omega}'\rightarrow\vec{\Omega})$, where

$$\sigma\left(\vec{\Omega}\right)=u_L G\left(\vec{\Omega}\right),\qquad \sigma_S\left(\vec{\Omega}'\rightarrow\vec{\Omega}\right)=u_L\pi^{-1}\Gamma\left(\vec{\Omega}'\rightarrow\vec{\Omega}\right). \quad (4)$$

[14] Equation (1) alone does not provide a full description of the transport process. Boundary conditions need to be specified. We ignore pulse interactions in the atmosphere. The bottom of the canopy is assumed to be a horizontally homogeneous Lambertian surface. On the basis of these assumptions, the boundary conditions can be written as

$$\begin{cases} I_\lambda\left(t,\vec{r}_{xy},0,\vec{\Omega}\right)=f_\lambda(t)\cdot\delta\left(\vec{\Omega}-\vec{\Omega}_0\right),\vec{r}_{xy}\in S_f, \quad \mu\left(\vec{\Omega}_0\right)<0,\\ I_\lambda\left(0,\vec{r},\vec{\Omega}\right)=0, \quad 0<z<H,\\ I_\lambda\left(t,\vec{r}_{xy},H,\vec{\Omega}\right)=\frac{\rho_{soil}(\lambda)}{\pi}\int\limits_{2\pi^-}I_\lambda\left(t,\vec{r}_{xy},H,\vec{\Omega}'\right)\cdot\left|\mu\left(\vec{\Omega}'\right)\right|d\vec{\Omega}', \quad \mu\left(\vec{\Omega}\right)>0,\end{cases} \quad (5)$$

where $\vec{\Omega}_0$ is the direction of incoming radiation; $\mu(\vec{\Omega})$ is the cosine of the polar angle of direction $\vec{\Omega}$; $f_\lambda(t)$ is a function characterizing pulse intensity; S_f is a footprint area; $\rho_{soil}(\lambda)$ and is the soil hemispherical reflectance. For simplicity, we will omit the symbol λ denoting the wavelength dependence in further notations.

[15] Most of the existing approaches use a single scattering approximation to the boundary value problem (1), (5) [e.g., *Sun and Ranson*, 2000; *Ni-Meister et al.*, 2001]. Its solution defines the attenuation of incoming radiation with depth. The number of photons reaching a level z without suffering a collision and reflected directly back is calculated. The moment at which backscattered energy from the level z will reach the sensor is assigned to twice the time photons take to reach the level z. As a result, a record of backscattered energy as a function of time is obtained.

[16] *Sun and Ranson* [2000] used a similar approach for their return signal simulation model. They tested the model with data collected in the old jack pine stand at the BOREAS Southern Study Area. The lack of calibration of the SLICER signal and the uncertainty of lidar footprint position prevented direct comparisons between the measured and simulated waveforms. However, comparisons of the averaged SLICER waveforms and the model simulations for the same area proved to be useful. The model accounts for single scattering only. The authors relied on the results of the simulations of *Blair and Hofton* [1999], who asserted that the multiple scattering was not a significant contributor to the waveforms. However, the authors admitted that the slower decay of the lidar waveform compared to the simulated return signal may be due to the presence of multiple scattering.

[17] In this paper, we will estimate the contribution of multiple scattering radiation to the SLICER waveforms through the solution of the time-dependent RT equation (equation (1)). A return waveform will be calculated as the upward reflected radiation at the top of the canopy.

3. Mean Characteristics of the Three-Dimensional Radiation Field

[18] Lidar sensors onboard aircrafts measure the amount of radiation intensity coming from an area exceeding the laser footprint, for example, for the SLICER instrument, the area covered by the telescope field-of-view is five times as much as the footprint area. The SLICER footprint distribution pattern on the ground is a track of footprints consisting

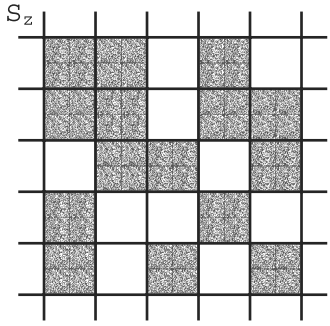

Figure 2a. An illustration for the definition of the probability function p(z). This function defines the probability of finding foliage elements in a horizontal plane S_z at depth z. Plane S_z can be thought as a grid with randomly foliated cells, and p(z) is the number of foliated cells to the total number of cells at depth z. For this picture, p(z) = 0.6.

of five contiguous footprint lines along the direction of flight [*Harding et al.*, 2000].

[19] In any signal propagation model, it is desirable to calculate the mean radiation field directly. Here we adopt a model of mean intensity proposed by *Vainikko* [1973a, 1973b]. Let S_z be a sufficiently large area over a horizontal plane at depth z. Two kinds of mean intensity will be evaluated:

[20] (1) the mean intensity of radiation over a horizontal plane at depth z, i.e.,

$$\bar{I}\left(t, z, \vec{\Omega}\right) = \frac{\iint_{S_z} I\left(t, x, y, z, \vec{\Omega}\right) dxdy}{\iint_{S_z} dxdy}; \tag{6}$$

[21] (2) the mean intensity of radiation over a vegetated area at depth z, i.e.,

$$U\left(t, z, \vec{\Omega}\right) = \frac{\iint_{S_z} \chi(x, y, z) I\left(t, x, y, z, \vec{\Omega}\right) dxdy}{\iint_{S_z} \chi(x, y, z) dxdy}. \tag{7}$$

[22] Two important issues related to equations (6)–(7) need to be addressed. First, the integration is performed over the area approximately equal to the laser footprint area with 8.4–9.0 m in diameter for the coniferous sites and 10.4–11.0 m for the deciduous sites. The diameter values exceed significantly the photon mean free path, which is proportional to $1/\sigma(\vec{\Omega})$ and defines the average distance at which leaves are separated from each other. Thus the conception of mean intensity is applicable here. Second, the spatial distribution of laser energy across the footprint has a circular, Gaussian distribution [*Harding et al.*, 2000]. In this study, we approximate the Gaussian distribution with a uniform distribution in order to satisfy the requirements of a stochastic model. The total amount of energy within the footprint area remains the same. It should be noted that, in a general case, Gaussian and uniform distributions of incident energy would lead to different forms of the return. Within our approach, however, a layer within vegetation is treated as a horizontal surface with averaged parameters characterizing its reflection and transmission properties. Thus the model is sensitive only to the total amount of radiation incident at each layer and the Gaussian distribution can be replaced with the uniform.

[23] The vertical heterogeneity of vegetation is described by the leaf vertical foliage density function

$$p(z) = \frac{\iint_{S_z} \chi(x, y, z) dxdy}{\int_{S_z} dxdy}, \tag{8}$$

which is the probability of finding foliage elements at level z (Figure 2a). In terms of this notation, the leaf area index (one-sided leaf area per unit ground area) is

$$LAI = u_L \int_0^H p(z) dz. \tag{9}$$

The correlation between foliage elements in different layers is described by

$$q\left(z, \xi, \vec{\Omega}\right) = \frac{\iint_{S_z} \chi(\vec{r}) \chi\left(\vec{r} - \zeta\vec{\Omega}\right) dxdy}{\int_{S_z} dxdy}, \tag{10}$$

which is the probability of finding simultaneously vegetated elements at two points $\vec{r} \in S_z$ and $\vec{r} \in S_\xi$ at distance $\zeta = |z - \xi|/\mu(\vec{\Omega})$ along the direction $\vec{\Omega}$. Later, we shall use another function,

$$K\left(z, \xi, \vec{\Omega}\right) = \frac{q\left(z, \xi, \vec{\Omega}\right)}{p(z)}, \tag{11}$$

which is the conditional probability of finding a vegetated element at two points $\vec{r} \in S_z$ and $\vec{r} - \zeta\vec{\Omega} \in S_\xi$ given that there is a leaf at $\vec{r} \in S_z$ (Figure 2b). When $z = \xi$, equation (10) describes the correlation of elements in the same layer.

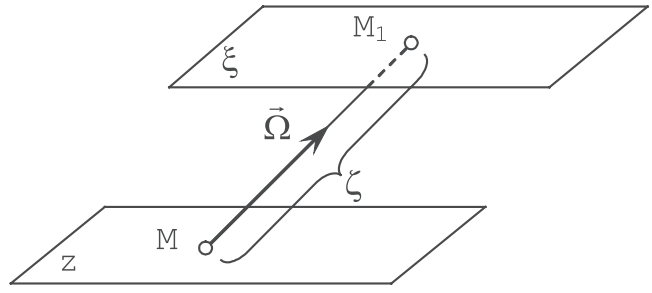

Figure 2b. An illustration for the definition of the conditional probability function K(z, ξ, $\vec{\Omega}$). This function defines the probability that one finds a vegetated element at point $M_1(\mu, \eta, \xi)$, moving from point M(x, y, z) along the direction $\vec{\Omega}$, given that there is a vegetated element at M(x, y, z).

[24] A procedure to derive equations for the mean intensities $\bar{I}(t,z,\vec{\Omega})$ and $\bar{U}(t,z,\vec{\Omega})$ in the case of time-independent transport was initially proposed by *Vainikko* [1973a, 1973b] for broken clouds, and applied to vegetation by *Shabanov et al.* [2000]. In this paper, we extend this technique to derive a system of time-dependent equations for the mean intensities.

[25] The derivation is a two-step process [*Shabanov et al.*, 2000]. First, integration of equation (1) along the line $(\vec{r}_{top}-\zeta\vec{\Omega})$ for downward directions and along $(\vec{r}_{bottom}+\zeta\vec{\Omega})$ for upward directions allows expansion of the streaming operator $\vec{\Omega}\bullet\nabla$. Second, the resulting equations are averaged over a horizontal plane S_z and over its vegetated part. The final system of equations for the mean intensity of radiation over a horizontal plane

$$\begin{cases} \bar{I}\left(t,z,\vec{\Omega}\right)+\dfrac{1}{\left|\mu\left(\vec{\Omega}\right)\right|}\cdot\displaystyle\int_0^z\sigma\left(\vec{\Omega}\right)\cdot p(\xi)\cdot U\left(t,\xi,\vec{\Omega}\right)d\xi+\dfrac{1}{\left|\mu\left(\vec{\Omega}\right)\right|}\cdot\dfrac{1}{c}\cdot\dfrac{\partial}{\partial t}\displaystyle\int_0^z\bar{I}\left(t,\xi,\vec{\Omega}\right)d\xi \\ =\dfrac{1}{\left|\mu\left(\vec{\Omega}\right)\right|}\cdot\displaystyle\int_0^z d\xi\cdot p(\xi)\cdot\int_{4\pi}\sigma_S\left(\vec{\Omega}'\to\vec{\Omega}\right)U\left(t,\xi,\vec{\Omega}'\right)d\vec{\Omega}'+\bar{I}\left(t,0,\vec{\Omega}\right), \quad \mu(\Omega)<0, \\ \bar{I}\left(t,z,\vec{\Omega}\right)+\dfrac{1}{\mu(\Omega)}\cdot\displaystyle\int_z^H\sigma\left(\vec{\Omega}\right)\cdot p(\xi)\cdot U\left(t,\xi,\vec{\Omega}\right)d\xi+\dfrac{1}{\mu(\Omega)}\cdot\dfrac{1}{c}\cdot\dfrac{\partial}{\partial t}\displaystyle\int_z^H\bar{I}\left(t,\xi,\vec{\Omega}\right)d\xi \\ =\dfrac{1}{\mu(\Omega)}\cdot\displaystyle\int_z^H d\xi\cdot p(\xi)\cdot\int_{4\pi}\sigma_S\left(\vec{\Omega}'\to\vec{\Omega}\right)\cdot U\left(t,\xi,\vec{\Omega}'\right)d\vec{\Omega}'+\bar{I}\left(t,H,\vec{\Omega}\right), \quad \mu(\Omega)>0, \end{cases} \tag{12}$$

and for the mean intensity over a vegetated area,

$$\begin{cases} U\left(t,z,\vec{\Omega}\right)+\dfrac{1}{\left|\mu\left(\vec{\Omega}\right)\right|}\cdot\displaystyle\int_0^z\sigma\left(\vec{\Omega}\right)\cdot K\left(z,\xi,\vec{\Omega}\right)\cdot U\left(t,\xi,\vec{\Omega}\right)d\xi+\dfrac{1}{\left|\mu\left(\vec{\Omega}\right)\right|}\cdot\dfrac{1}{c}\cdot\dfrac{\partial}{\partial t}\displaystyle\int_0^z U\left(t,\xi,\vec{\Omega}\right)d\xi \\ =\dfrac{1}{\left|\mu\left(\vec{\Omega}\right)\right|}\cdot\displaystyle\int_0^z d\xi\cdot K\left(z,\xi,\vec{\Omega}\right)\cdot\int_{4\pi}\sigma_S\left(\vec{\Omega}'\to\vec{\Omega}\right)\cdot U\left(t,\xi,\vec{\Omega}'\right)d\vec{\Omega}'+I\left(t,0,\vec{\Omega}\right), \quad \mu(\Omega)<0, \\ U\left(t,z,\vec{\Omega}\right)+\dfrac{1}{\mu(\Omega)}\cdot\displaystyle\int_z^H\sigma\left(\vec{\Omega}\right)\cdot K\left(z,\xi,\vec{\Omega}\right)\cdot U\left(t,\xi,\vec{\Omega}\right)d\xi+\dfrac{1}{\mu(\Omega)}\cdot\dfrac{1}{c}\cdot\dfrac{\partial}{\partial t}\displaystyle\int_z^H U\left(t,\xi,\vec{\Omega}\right)d\xi \\ =\dfrac{1}{\mu(\Omega)}\cdot\displaystyle\int_z^H d\xi\cdot K\left(z,\xi,\vec{\Omega}\right)\cdot\int_{4\pi}\sigma_S\left(\vec{\Omega}'\to\vec{\Omega}\right)\cdot U\left(t,\xi,\vec{\Omega}'\right)d\vec{\Omega}'+I\left(t,H,\vec{\Omega}\right), \quad \mu(\Omega)>0. \end{cases} \tag{13}$$

[26] The averaging procedure leads to a parameterization of the stochastic equations in terms of the leaf vertical foliage density p(z) and the correlation $K(z,\xi,\vec{\Omega})$ between leaves in different layers. In the absence of correlation, the coefficient $K(z,\xi,\vec{\Omega})$ simplifies to

$$K\left(z,\xi,\vec{\Omega}\right)=\frac{p(z)p(\xi)}{p(z)}=p(\xi). \tag{14}$$

In this case, the solution of equation (12) coincides with the solution of equation (13), i.e., $\bar{I}(t,z,\vec{\Omega})=U(t,z,\vec{\Omega})$, and the radiative transfer process is described by the one-dimensional transport equation. However, this is only a limiting case. In general, both mean intensities are required to account for the correlation between leaves in different layers, which cannot be approximated by the one-dimensional transport equation.

3.1. Direct and Diffuse Components of U (t,z,$\vec{\Omega}$)

[27] We express the solution of equation (13) as the sum of direct and diffuse components, that is,

$$U\left(t,z,\vec{\Omega}\right)=U_\delta(t,z)\cdot\delta\left(\vec{\Omega}-\vec{\Omega}_0\right)+U_d\left(t,z,\vec{\Omega}\right). \tag{15}$$

The direct component $U_\delta(t, z)$ represents those photons, which interact with leaves at depth z without experiencing a collision in the layer [0, z]. The diffuse component function $U_d(t, z, \vec{\Omega})$ specifies diffuse radiation field due to scattering by vegetation elements.

[28] Substituting equation (15) into equation (13) and separating the terms with $\delta(\vec{\Omega}-\vec{\Omega}_0)$ results in an equation for the direct component,

$$U_\delta(t,z)+\frac{\sigma\left(\vec{\Omega}_0\right)}{\left|\mu\left(\vec{\Omega}_0\right)\right|}\int_0^z K\left(z,\xi,\vec{\Omega}_0\right)U_\delta(t,\xi)d\xi + \frac{1}{\left|\mu\left(\vec{\Omega}_0\right)\right|}\frac{1}{c}\frac{\partial}{\partial t}\int_0^z U_\delta(t,\xi)d\xi=f(t), \tag{16}$$

where f(t) characterizes the intensity of incoming radiation (see equation (5)). The diffuse component, $U_d(t, z, \vec{\Omega})$, satisfies the following equations

$$\begin{cases} U_d\left(t,z,\vec{\Omega}\right)+\dfrac{\sigma\left(\vec{\Omega}\right)}{|\mu(\Omega)|}\displaystyle\int_0^z K\left(z,\xi,\vec{\Omega}\right)U_d\left(t,\xi,\vec{\Omega}\right)d\xi+\dfrac{1}{\left|\mu\left(\vec{\Omega}\right)\right|}\dfrac{1}{c}\dfrac{\partial}{\partial t}\displaystyle\int_0^z U_d\left(t,\xi,\vec{\Omega}\right)d\xi \\ =\dfrac{1}{\left|\mu\left(\vec{\Omega}\right)\right|}\displaystyle\int_0^z K\left(z,\xi,\vec{\Omega}\right)S\left(t,\xi,\vec{\Omega}\right)d\xi+\dfrac{\sigma_S\left(\vec{\Omega}_0\to\vec{\Omega}\right)}{\left|\mu\left(\vec{\Omega}\right)\right|}\displaystyle\int_0^z K\left(z,\xi,\vec{\Omega}\right)U_\delta(t,\xi)d\xi, \quad \mu\left(\vec{\Omega}\right)<0, \\ U_d\left(t,z,\vec{\Omega}\right)+\dfrac{\sigma\left(\vec{\Omega}\right)}{\mu\left(\vec{\Omega}\right)}\displaystyle\int_z^H K\left(z,\xi,\vec{\Omega}\right)U_d\left(t,\xi,\vec{\Omega}\right)d\xi+\dfrac{1}{\mu\left(\vec{\Omega}\right)}\dfrac{1}{c}\dfrac{\partial}{\partial t}\displaystyle\int_z^H U_d\left(t,\xi,\vec{\Omega}\right)d\xi \\ =\dfrac{1}{\mu\left(\vec{\Omega}\right)}\displaystyle\int_z^H K\left(z,\xi,\vec{\Omega}\right)S\left(t,\xi,\vec{\Omega}\right)d\xi+\dfrac{\sigma_S\left(\vec{\Omega}_0\to\vec{\Omega}\right)}{\mu\left(\vec{\Omega}\right)}\displaystyle\int_z^H K\left(z,\xi,\vec{\Omega}\right)U_\delta(t,\xi)d\xi \\ +I\left(t,H,\vec{\Omega}\right), \quad \mu\left(\vec{\Omega}\right)>0. \end{cases} \tag{17}$$

Here

$$S\left(t,\xi,\vec{\Omega}\right)=\int_{4\pi}\sigma_S\left(\vec{\Omega}'\to\vec{\Omega}\right)U_d\left(t,\xi,\vec{\Omega}'\right)d\vec{\Omega}' \tag{18}$$

is the source function describing the contribution of multiply scattered radiation. When the source function is 0, the system of equations (17) describes the distribution of photons scattered just once.

3.2. Direct and Diffuse Components of $\bar{I}$ (t,z,$\vec{\Omega}$)

[29] Analogous to the technique applied earlier, we represent the mean intensity of radiation over a horizontal plane as the sum of the direct $I_\delta(t, z)$ and diffuse $I_\delta(t, z, \vec{\Omega})$ components,

$$\bar{I}\left(t,z,\vec{\Omega}\right)=\bar{I}_\delta(t,z)\cdot\delta\left(\vec{\Omega}-\vec{\Omega}_0\right)+\bar{I}_d\left(t,z,\vec{\Omega}\right). \tag{19}$$

The substitution of equation (19) into equation (12) results in two equations. The first represents photons arriving at z without experiencing a collision. It satisfies the equation

$$\bar{I}_\delta(t,z)+\frac{\sigma\left(\vec{\Omega}_0\right)}{\left|\mu\left(\vec{\Omega}_0\right)\right|}\int_0^z p(\xi)U_\delta(t,\xi)d\xi + \frac{1}{\left|\mu\left(\vec{\Omega}_0\right)\right|}\frac{1}{c}\frac{\partial}{\partial t}\int_0^z \bar{I}_\delta(t,\xi)dx=f(t). \tag{20}$$

The second specifies the diffuse radiation field due to multiply scattered radiation,

$$\begin{cases} \bar{I}_d\left(t,z,\vec{\Omega}\right)+\dfrac{\sigma\left(\vec{\Omega}\right)}{|\mu(\Omega)|}\displaystyle\int_0^z p(\xi)U_d\left(t,\xi,\vec{\Omega}\right)d\xi+\dfrac{1}{\left|\mu\left(\vec{\Omega}\right)\right|}\dfrac{1}{c}\dfrac{\partial}{\partial t}\displaystyle\int_0^z \bar{I}_d\left(t,\xi,\vec{\Omega}\right)d\xi \\ =\dfrac{1}{\left|\mu\left(\vec{\Omega}\right)\right|}\displaystyle\int_0^z p(\xi)S\left(t,\xi,\vec{\Omega}\right)d\xi+\dfrac{\sigma_S\left(\vec{\Omega}_0\to\vec{\Omega}\right)}{\left|\mu\left(\vec{\Omega}\right)\right|}\displaystyle\int_0^z p(\xi)U_\delta(t,\xi)d\xi, \quad \mu\left(\vec{\Omega}\right)>0, \\ \bar{I}_d\left(t,z,\vec{\Omega}\right)+\dfrac{\sigma\left(\vec{\Omega}\right)}{\mu\left(\vec{\Omega}\right)}\displaystyle\int_z^H p(\xi)U_d\left(t,\xi,\vec{\Omega}\right)d\xi+\dfrac{1}{\mu\left(\vec{\Omega}\right)}\dfrac{1}{c}\dfrac{\partial}{\partial t}\displaystyle\int_z^H \bar{I}_d\left(t,\xi,\vec{\Omega}\right)d\xi \\ =\dfrac{1}{\mu\left(\vec{\Omega}\right)}\displaystyle\int_z^H p(\xi)S\left(t,\xi,\vec{\Omega}\right)d\xi+\dfrac{\sigma_S\left(\vec{\Omega}_0\to\vec{\Omega}\right)}{\mu\left(\vec{\Omega}\right)}\displaystyle\int_z^H p(\xi)U_\delta(t,\xi)d\xi+I\left(t,H,\vec{\Omega}\right),\mu\left(\vec{\Omega}\right)>0. \end{cases} \tag{21}$$

As stated previously, $\bar{I}(t,z,\vec{\Omega})$ depends on the mean intensity over a vegetated area; therefore the equations for $U(t,z,\vec{\Omega})$ have to be first solved.

4. Numerical Scheme

[30] The model parameters such as pulse duration and signal vertical resolution are similar to the SLICER instrument parameters. The SLICER transmitter operates in the NIR at 1064 nm. Its laser pulse has a curved "Raleigh" shape and a width of 4 ns. The vertical resolution of recorded waveforms is 0.112 m. For this study, the SLICER signals were smoothed to obtain the resolution of 0.336 m. The amount of transmitted energy per pulse is 0.7 mJ [*Harding et al.*, 2000].

[31] The canopy is divided into n layers of thickness $\Delta z = 0.336$ m. The observation time is divided into m intervals $[t_{i-1}, t_i]$, $\Delta t = t_i - t_{i-1} = \Delta z/c$ (c is the speed of light). The simulated Raleigh pulse is divided into k narrow pulses of duration Δt. At each moment t_i, i = 0,. . ., m, the intensity of incoming radiation is equal to the pulse amplitude at that moment.

[32] To discretize equation (16), it is integrated over $[t_{i-1}, t_i]$ and the obtained integrals are approximated with a trapezoidal quadrature scheme. Grouping the terms that depend on t_{i-1} together and designating them as $F_\delta\left(t_{i-1},z,\vec{\Omega}_0\right)$ results in an integral equation for U_δ at time t_i,

$$U_\delta(t_i,z)+\frac{\sigma\left(\vec{\Omega}_0\right)}{\left|\mu\left(\vec{\Omega}_0\right)\right|}\int_0^z K'\left(z,\xi,\vec{\Omega}_0\right)U_\delta(t_i,\xi)d\xi = f(t_i,\lambda)+F_\delta\left(t_{i-1},z,\vec{\Omega}_0\right), \tag{22}$$

where

$$K'\left(z,\xi,\vec{\Omega}_0\right)=K\left(z,\xi,\vec{\Omega}_0\right)+\left(cW_t\sigma\left(\vec{\Omega}_0\right)\right)^{-1}. \tag{23}$$

Here $W_t \sim \Delta t$ is the weight that depends on the numerical scheme used to approximate the integrals over the interval $[t_{i-1}, t_i]$. Given $F_\delta(t_{i-1},z,\vec{\Omega}_0)$ and $f(t_i)$, the integral equation (22) can be numerically solved for $U_\delta(t, z)$. The general form of a numerical scheme is represented in Appendix A.

[33] Applying a similar integration procedure to equation (17) results in

$$\begin{cases} U_d\left(t_i,z,\vec{\Omega}\right)+\dfrac{\sigma\left(\vec{\Omega}\right)}{\left|\mu\left(\vec{\Omega}\right)\right|}\displaystyle\int_0^z=K'\left(z,\xi,\vec{\Omega}\right)U_d\left(t_i,\xi,\vec{\Omega}\right)d\xi=\dfrac{1}{\left|\mu\left(\vec{\Omega}\right)\right|}\displaystyle\int_0^z K\left(z,\xi,\vec{\Omega}\right)S\left(t_i,\xi,\vec{\Omega}\right)d\xi \\ +\dfrac{\sigma_S\left(\vec{\Omega}_0\to\vec{\Omega}\right)}{\left|\mu\left(\vec{\Omega}\right)\right|}\displaystyle\int_0^z K\left(z,\xi,\vec{\Omega}\right)U_\delta(t_i,\xi)d\xi+F_d\left(t_{i-1},z,\vec{\Omega}\right), \quad \mu\left(\vec{\Omega}\right)<0, \\ U_d\left(t_i,z,\vec{\Omega}\right)+\dfrac{\sigma\left(\vec{\Omega}\right)}{\mu\left(\vec{\Omega}\right)}\displaystyle\int_z^H K'\left(z,\xi,\vec{\Omega}\right)U_d\left(t_i,\xi,\vec{\Omega}\right)d\xi=\dfrac{1}{\mu\left(\vec{\Omega}\right)}\displaystyle\int_{z^H} K\left(z,\xi,\vec{\Omega}\right)S\left(t_i,\xi,\vec{\Omega}\right)d\xi \\ +\dfrac{\sigma_S\left(\vec{\Omega}_0\to\vec{\Omega}\right)}{\mu\left(\vec{\Omega}\right)}\displaystyle\int_z^H K\left(z,\xi,\vec{\Omega}\right)U_\delta(t_i,\xi)d\xi+F_d\left(t_{i-1},z,\vec{\Omega}\right)+I_d\left(t_i,H,\vec{\Omega}\right), \quad \mu\left(\vec{\Omega}\right)>0. \end{cases} \tag{24}$$

Given F_d at time t_{i-1}, we solve the integral equation (24) for U_d at time t_i using the successive orders of scattering approximations [*Shabanov et al.*, 2000]. The *n*th approximation to the solution is given by

$$U_d^n\left(t_i,z,\vec{\Omega}\right)=J_1\left(t_i,z,\vec{\Omega}\right)+J_2\left(t_i,z,\vec{\Omega}\right)+...+J_n\left(t_i,z,\vec{\Omega}\right). \tag{25}$$

Function $J_k(t_i, z, \vec{\Omega})$, k = 1,2,...,n, is the mean intensity of photons scattered k times at time t_i. It satisfies the following equations

$$\begin{aligned} &J_k\left(t_i,z,\vec{\Omega}\right)+\frac{\sigma\left(\vec{\Omega}\right)}{\left|\mu\left(\vec{\Omega}\right)\right|}\int_0^z K'\left(z,\xi,\vec{\Omega}\right)J_k\left(t_i,\xi,\vec{\Omega}\right)d\xi \\ &\quad=R_{k-1}\left(t_i,z,\vec{\Omega}\right)+G_k\left(t_{i-1},z,\vec{\Omega}\right), \quad \mu\left(\vec{\Omega}\right)<0, \\ &J_k\left(t_i,z,\vec{\Omega}\right)+\frac{\sigma\left(\vec{\Omega}\right)}{\mu\left(\vec{\Omega}\right)}\int_z^H K'\left(z,\xi,\vec{\Omega}\right)J_k\left(t_i,\xi,\vec{\Omega}\right)d\xi \\ &\quad=R_{k-1}\left(t_i,z,\vec{\Omega}\right)+G_k\left(t_{i-1},z,\vec{\Omega}\right), \quad \mu\left(\vec{\Omega}\right)>0. \end{aligned} \tag{26}$$

In the above,

$$\begin{aligned} R_0\left(t_i,z,\vec{\Omega}\right)&=\frac{\sigma_S\left(\vec{\Omega}_0\to\vec{\Omega}\right)}{\left|\mu\left(\vec{\Omega}\right)\right|}\int_0^z K\left(z,\xi,\vec{\Omega}\right)U_\delta(t_i,\xi)d\xi, \\ &\qquad \mu\left(\vec{\Omega}\right)<0, \\ R_0\left(t_i,z,\vec{\Omega}\right)&=\frac{\sigma_S\left(\vec{\Omega}_0\to\vec{\Omega}\right)}{\mu\left(\vec{\Omega}\right)}\int_z^H K\left(z,\xi,\vec{\Omega}\right) \\ &\qquad \cdot U_\delta(t_i,\xi)d\xi+U_d\left(t_i,H,\vec{\Omega}\right), \qquad \mu\left(\vec{\Omega}\right)<0, \end{aligned} \tag{27}$$

and

$$\begin{aligned} R_k\left(t_i,z,\vec{\Omega}\right)&=\frac{1}{\left|\mu\left(\vec{\Omega}\right)\right|}\int_0^z K\left(z,\xi,\vec{\Omega}\right)S_k\left(t_i,\xi,\vec{\Omega}\right)d\xi, \\ &\qquad \mu\left(\vec{\Omega}\right)<0, \quad k\geq 1, \\ R_k\left(t_i,z,\vec{\Omega}\right)&=\frac{1}{\mu\left(\vec{\Omega}\right)}\int_0^z K\left(z,\xi,\vec{\Omega}\right)S_k\left(t_i,\xi,\vec{\Omega}\right)d\xi, \\ &\qquad \mu\left(\vec{\Omega}\right)<0, \quad k\geq 1, \\ S_k\left(t_i,z,\vec{\Omega}\right)&=\int_{4\pi}\sigma_S\left(\vec{\Omega}'\to\vec{\Omega}\right)J_k\left(t_i,z,\vec{\Omega}'\right)d\vec{\Omega}'. \end{aligned} \tag{28}$$

A numerical scheme for equation (26) is given in Appendix A. The source function $S_k(t_i, z, \vec{\Omega})$ is approximated by the Carlson quadrature [*Shabanov et al.*, 2000, *Germogenova*, 1986].

[34] The discretization of the equation for the mean intensity over a horizontal plane can be performed in a similar manner. The equation for the direct component is

$$\bar{I}_\delta(t_i, z) + \frac{1}{cW_t\left|\mu\left(\vec{\Omega}_0\right)\right|}\int_0^z \bar{I}_\delta(t_i, \xi)d\xi + \frac{\sigma\left(\vec{\Omega}_0\right)}{\left|\mu\left(\vec{\Omega}_0\right)\right|}\int_0^z p(\xi)U_\delta(t_i, \xi)d\xi = f(t_i) + G_\delta\left(t_{i-1}, z, \vec{\Omega}_0\right). \quad (29)$$

The discretized system of equations for the diffuse component has the following form:

$$\begin{cases} \bar{I}_d\left(t_i, z, \vec{\Omega}\right) + \frac{1}{cW_t\left|\mu\left(\vec{\Omega}\right)\right|}\int_0^z \bar{I}_d\left(t_i, \xi, \vec{\Omega}\right)d\xi = G_d\left(t_{i-1}, z, \vec{\Omega}\right) \\ + \frac{1}{\left|\mu\left(\vec{\Omega}\right)\right|}\int_0^z \left[-\sigma\left(\vec{\Omega}\right)U_d\left(t_i, \xi, \vec{\Omega}\right) + \sigma_S\left(\vec{\Omega}_0 \to \vec{\Omega}\right)U_\delta(t_i, \xi) + S\left(t_i, \xi, \vec{\Omega}\right)\right]p(\xi)d\xi,\ \mu\left(\vec{\Omega}\right) < 0, \\ \bar{I}_d\left(t_i, z, \vec{\Omega}\right) + \frac{1}{cW_t\mu\left(\vec{\Omega}\right)}\int_z^H \bar{I}_d\left(t_i, \xi, \vec{\Omega}\right)d\xi = G_d\left(t_{i-1}, z, \vec{\Omega}\right) + \frac{1}{\mu\left(\vec{\Omega}\right)}\int_z^H \left[-\sigma\left(\vec{\Omega}\right)U_d\left(t_i, \xi, \vec{\Omega}\right)\right. \\ \left. + \sigma_S\left(\vec{\Omega}_0 \to \vec{\Omega}\right)U_\delta(t_i, \xi) + S\left(t_i, \xi, \vec{\Omega}\right)\right]p(\xi)d\xi,\ \mu\left(\vec{\Omega}\right) < 0. \end{cases} \quad (30)$$

Equations (29)–(30) are straightforward numerical integrations of the equations for $U(t_i, z, \vec{\Omega}_0)$.

5. Evaluation of the Model

[35] The model was tested with data from needle and broadleaf forests. We also provide a sensitivity study to illustrate the dependence of the mean intensities on the duration of incoming radiation flux and the number of iterations. The model predictions are compared to SLICER signals for different forest types.

[36] The input variables are: (1) characteristics of incoming radiation: direction, intensity, and pulse duration; (2) canopy structural parameters: tree height H, crown length L, leaf area density u_L, leaf normal orientation distribution (uniform, planophile, erectrophile, etc. [*Ross*, 1981]), statistical probability functions p(z) and $K(z, \xi, \vec{\Omega})$ defined earlier by equation (8) and equation (11); (3) optical properties of leaves and soil: leaf hemispherical reflectance and transmittance, soil hemispherical reflectance ρ_{soil}.

[37] Function p(z) is modeled on the basis of the assumption of hemi-ellipsoid crown shapes and field-measured values of LAI:

$$p(z) = p_0\left(1 - (z - L)^2/L^2\right), \quad (31)$$

where $p_0 = 3LAI/(2Lu_L)$, as defined from equation (9). Small variation of p values (within 10%) was used to provide a more realistic representation of canopy structure. Function $K(z, \xi, \vec{\Omega})$, which describes the correlation of leaves in different layers, strongly depends on the foliage clumping. In the absence of clumping, leaves can be considered uniformly distributed within a layer and K function is defined by equation (4). The ability of leaves to clump is described with a clumping index, which is 0.5 for coniferous and 0.7 for deciduous forests [*Chen et al.*, 1997]. Thus, to account for clumping, K function can be modeled as

$$K\left(z, \xi, \vec{\Omega}\right) = \frac{p(z)p(\xi)\beta}{p(z)} = p(\xi)\cdot\beta \quad (32)$$

Clumping reduces the probability of finding vegetated elements in two layers simultaneously moving along a given direction.

[38] The model outputs include: (1) temporal variation of the direct components of the mean intensities, $\bar{I}_\delta(t, z)$ and $U_\delta(t, z)$, as functions of z; and (2) angular and temporal distributions of the diffuse components, $\bar{I}_d\left(t, z, \vec{\Omega}\right)$ and $U_d(t, z, \vec{\Omega})$, as functions of z.

5.1. Sensitivity Study

[39] The sensitivity study described here consists of two parts. First, the behavior of the model is studied for the case of infinite laser pulse duration. Second, the sensitivity of the model to the number of iterations is assessed. The parameters used in this study are: H = 10 m, L = 6.7 m, $G(\vec{\Omega}) = 0.5$ (uniform leaf distribution), p(z) and $\bar{K}\left(z, \xi, \vec{\Omega}\right)$ are modeled according to equations (31)–(32), $\rho_L = 0.41$, $\tau_L = 0.32$, and $\rho_{soil} = 0.303$. The area scattering phase function used in equation (4) is calculated as $\Gamma\left(\vec{\Omega}' \to \vec{\Omega}\right) = \frac{\omega_L}{3\pi}(\sin\beta - \beta\cos\beta) + \frac{\tau_L}{\pi}\cos\beta$, where $\beta = \arccos\left(\vec{\Omega}'\cdot\vec{\Omega}\right)$ and $\omega_L = \rho_L + \tau_L$ is the leaf albedo [*Shultis and Myneni*, 1988]. The tree structural and optical parameters were estimated from field measurements at the BOREAS southern old black spruce site [*Chen et al.*, 1997; *Middleton et al.*, 1997; *Ni-Meister et al.*, 2001]. They will also be used later in Section 5.2 for the second SOBS plot.

[40] First, if a constant photon flux is incident on the top of vegetation over a long period of time, the solution of the time-dependent RTE approaches its stationary limit. Such a regime is described by the time-independent RT equation [*Shabanov et al.*, 2000]. Figure 3 illustrates the time distribution of diffuse radiation at the top of vegetation calculated with the time-dependent and time-independent models. It requires about 60 ns to reach the stationary limit in this particular case. After this time, the outputs of the two

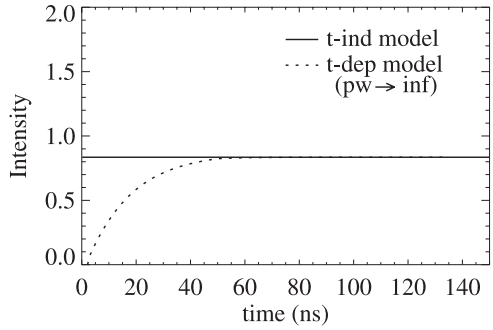

Figure 3. Upward diffuse radiation at the top of vegetation as a function of time. The solid line represents the input of the time-independent model. The dotted line is the input of the time-dependent model when the pulse width approaches infinity (pw → inf).

models become indistinguishable. Figure 3 also demonstrates that the use of a steady state radiative transfer in optical remote sensing is valid. Indeed, the time for radiation to propagate through the system (tens of ns) is short compared to variations in illumination conditions (typically, tens of minutes). The ability of the model to describe nonstationary and stationary radiation regimes makes it useful for interpretation of both active and passive remote sensing data.

[41] Second, the contribution of photons scattered n times to the radiation regime at a given moment of time is evaluated. The integral

$$E_n(t) = \int_0^L dz \int_{4\pi} J_n\left(t, z, \vec{\Omega}\right) d\vec{\Omega} \tag{33}$$

is taken as a measure of the number of photons with n interactions within the vegetation canopy at moment t. Here $J_n(t_i, z, \vec{\Omega})$ is the intensity of photons scattered n times (see equations (25)–(28)).

[42] Figures 4a and 4b show the ratios $-\ln\frac{E_n(t)}{E_1(t)}$ and $-\ln\frac{E_{n+1}(t)}{E_n(t)}$ as functions of the scattering order n for different instants of time. The former shows the contribution of multiply scattered radiation with respect to a single scattering field, while the latter is the rate at which multiply scattered photons contribute to the radiation field. One can see that the contribution of high-order scattering decreases rapidly for $t \leq 17$ ns. However, multiple interactions can be quite significant for $t > 17$ ns. Note that the ratio $\frac{E_{n+1}(t)}{E_n(t)}$ tends to a time-independent constant value ρ. It follows from this property that, for a sufficiently large n, all curves can be asymptotically replaced by lines:

$$-\ln\frac{E_n(t)}{E_1(t)} = -n\ln\rho - \ln c(t), \tag{34}$$

where $-\ln \rho$ is the slope ratio, and $-\ln c(t)$ is a function characterizing the shift of the plotted curves with time. The curves produced for the larger t values the ratio $-\ln\frac{E_n(t)}{E_1(t)}$ first decreases for small n. It describes the situation when $E_n(t) > E_1(t)$. For the time-independent case, the maximum number

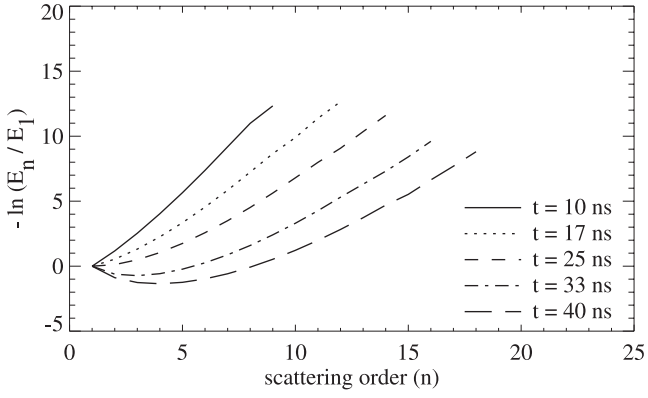

Figure 4a. Contribution of photons scattered n times for different time moments (t = 10, 17, 25, 33, and 40 ns). The laser pulse is assumed to be incident at the top of vegetation at time t = 0. Functions E_1 and E_n are defined by equation (33).

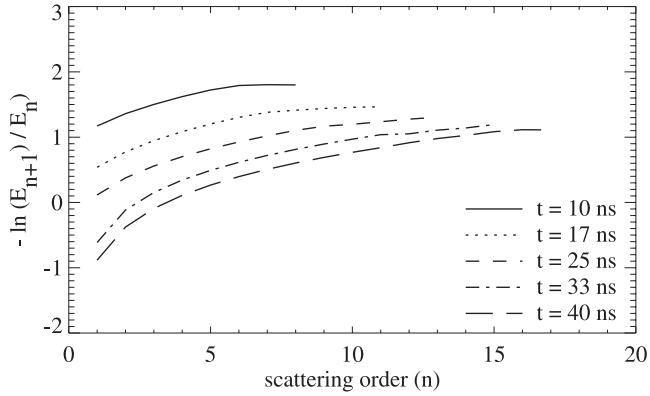

Figure 4b. The ratio $-\ln\frac{E_{n+1}(t)}{E_n(t)}$ as a function of scattering order n for different time moments (t = 10, 17, 25, 33, and 40 ns). The laser pulse is assumed to be incident at the top of vegetation at time t = 0. Functions E_n and E_{n+1} are defined by equation (33).

of photons scattered n times would not change with time because of the constant input of radiation into the canopy. For the case described here, photon flux enters the canopy during a small period of time equal to the laser pulse duration. With time, some fraction of photons scattered only once leaves the canopy and number of photons scattered more times exceeds the number of singly scattered photons inside the canopy.

[43] It follows from equation (34) that, for a sufficiently large n, E_n can be approximated by

$$E_n(t) = E_1(t)\rho^n c(t). \tag{35}$$

Here ρ^n can be interpreted as the probability for a photon to be scattered n times and c(t) as a function characterizing the dependence on time. The rate of convergence of the SOSA method is defined as

$$E - E_n = E_{n+1} + E_{n+2} + \ldots = c(t)E_1\rho^{n+1}(1 + \rho + \ldots) = c(t)E_1\frac{\rho^{n+1}}{1-\rho}. \tag{36}$$

Thus the contribution of multiply scattered photons to the radiation field at a given instant of time is proportional to $\rho^n/(1-\rho)$. The higher the probability of scattering events, the higher the contribution of multiply scattered photons to the radiation field. In this example, about n = 10 iterations are required to obtain a relative accuracy of 10^{-3}.

5.2. Model Testing

[44] Four different forest sites covered during SLICER missions were chosen to validate the model. The characteristics of each site are summarized in Table 1. The group includes both coniferous and broadleaf species. Field data used for model validation are available from field campaigns conducted at these places [*Chen et al.*, 1999; *Middleton et al.*, 1997; *Harding et al.*, 2001; *Parker et al.*, 2001]. A short description of each site is presented below, followed by comparisons of model-simulated signals with SLICER waveforms.

Table 1. Characteristics of the Four Sites Used for Model Parameterization[a]

Site	Age, years	Density, stems/ha	Tree height H, m	Crown Length L, m	Leaf Reflectance ρ_L	Leaf Transmittance τ_L	LAI	Soil Reflectance ρ_{soil}
SOJP	60–75	1600–4000	16.5–18.5	11.0–12.3	0.53	0.32	2.61	0.330
SOBS	0–155	3700–5800	10.0–11.0	6.7–7.3	0.41	0.32	4.00	0.303
SERC (intermediate)	41	840	31.5–33.0	21.0–22.0	0.45	0.45	5.16	0.225
SERC (mature)	99	1187	32.0–36.5	21.3–24.3	0.45	0.45	5.26	0.225

[a]SOJP and SOBS are southern old jack pine and black spruce stands measured during the BOREAS field campaign in 1996. The SERC sites are mixed deciduous forest stands at the Smithsonian Environmental Research Center (SERC), with the overstory predominantly comprised of tulip poplar.

[45] The first two sites, SOJP (southern old jack pine) and SOBS (southern old black spruce) are located in the BOREAS southern study area in Saskatchewan, Canada. Jack pine (*Pinus banksiana*) and black spruce (*Picea mariana*) are among the major boreal tree species. They were the subjects of intensive field campaigns carried out in 1994 as part of BOREAS field activities. A field data set that includes forest age, stem density [*Chen et al.*, 1997], tree structural parameters (height, LAI [*Chen et al.*, 1997], crown length, foliage area volume density [*Ni-Meister et al.*, 2001]), and optical properties of leaves [*Middleton et al.*, 1997] and ground [*Ni-Meister et al.*, 2001], was used in this study. Leaf reflectance and transmittance were measured at 1000 nm, which is close to the SLICER wavelength (1064 nm). The reflectance of jack pine needles is higher than for black spruce needles. SLICER measurements were taken on 29 July 1996. The SLICER instrument was flown in a NASA C-130 aircraft over the BOREAS southern area, including OJP (53°55′ N, 104°42′ W) and OBS (53°59′ N, 105°07′ W) sites. We ignore tree growth during the 2-year period between the field and SLICER measurements.

[46] The other two sites are closed canopy stands located in a mixed deciduous forest at the Smithsonian Environmental Research Center (SERC, 38°53′ N, 76°33′ W), about 10 km south-southeast of Annapolis, Maryland, on the western shore of Chesapeake Bay [*Harding et al.*, 2001]. The overstory is predominately comprised of tulip poplar (*Liriodendron tulipifera*). The vertical structure and number of woody species vary significantly. The intermediate stand is a broad unimodal canopy consisting of 14 different species. The mature stand has a bimodal vertical leaf area structure and consists of 19 species. The gap fraction is relatively small: 0.05 for the intermediate stand and 0.02 for the mature stand. SLICER data for these sites were collected on 7 September 1995. Ground measurements were taken within two weeks after that [*Harding et al.*, 2001]. The trees were fully leaved at this time. Canopy structural parameters (forest age, stem density, tree heights and LAI) are listed in [*Harding et al.*, 2001]; crown lengths are assumed to be two third of tree heights [*Oliver and Larson*, 1990]; leaf optical properties are taken from [*Parker et al.*, 2001]. The ground surface is dominantly comprised of leaf litter with some bare soil and rare live foliage. The reflectance of the ground is assumed to be half that of the canopy.

[47] Figures 5a and 5b show the results of comparison between model-simulated signals and recorded waveforms for the four sites. For each of the sites, three SLICER waveforms were extracted. We chose waveforms with different shapes and approximately equal amplitude values. The selection was made among data from the three interior footprints; waveforms corresponding to the two outer footprint positions were discarded as anomalous because of misalignment between the scan pattern and the outer edges of the instruments receiver field-of-view [*Lefsky et al.*, 1999a]. The selected signals were normalized by the maximum return signal in each waveform. It is the ground return for SOBS and SOJP and the maximum canopy return for the SERC sites. The digitizer bin units were converted into distance, with one digitizer bin corresponding to 0.1112 m. A smoothing procedure was applied to the signals to provide a better viewing. Three adjacent bins were summed and the averaged value was taken. The ground return was identified as the last discrete return above the mean background noise level. The maximum value of the ground return was assigned a height of zero. Tree height is the distance between the maximum ground return and the first canopy return. As the plotted SLICER signals reveal different heights for the same forest stand, the tree heights and crown sizes used in model simulations were defined for each signal individually. Table 1 shows the range of these parameters for the selected signals.

[48] The gap fraction is high in the coniferous stands and the ground return is well pronounced. It consists mainly of singly scattered photons capable of reaching the ground because of the gaps in the canopy, and some fraction of multiply scattered photons. The unimodal shapes of the SOJP and SOBS SLICER waveforms imply the absence of secondary forest understory. The third SOBS plot reveals some understory, seen as a small wide spike near the maximum return. For the first SOBS plot, the amplitude of the SLICER signal is greater than that in the simulations. Differences in foliage density affect the strength of the SLICER signals, while the model simulations assume a constant value. The agreement between the SLICER signals and model simulations is better for the signals with a slow decay of the waveform.

[49] The SOBS SLICER signals shown in Figure 5a were collected over the region where ground measurements described by *Chen et al.* [1997] were made. For the SOJP site, none of the SLICER tracks coincides with the location of *Chen et al.*'s measurements. Two SLICER tracks cross the area of another field campaign described in [*Sun and Ranson*, 2000]. The data from these tracks are used here.

[50] For the SERC forest stands, the SLICER data sets include regions where ground measurements were taken. Several subpeaks of canopy return, and small or even undistinguishable ground returns are typical for the waveforms collected over both mature and intermediate stands. The signals with identifiable ground returns were chosen to calculate tree heights. Only relatively unimodal waveform profiles are represented in Figure 5b, for the model does not include multimodel vegetation structure. Some small under-

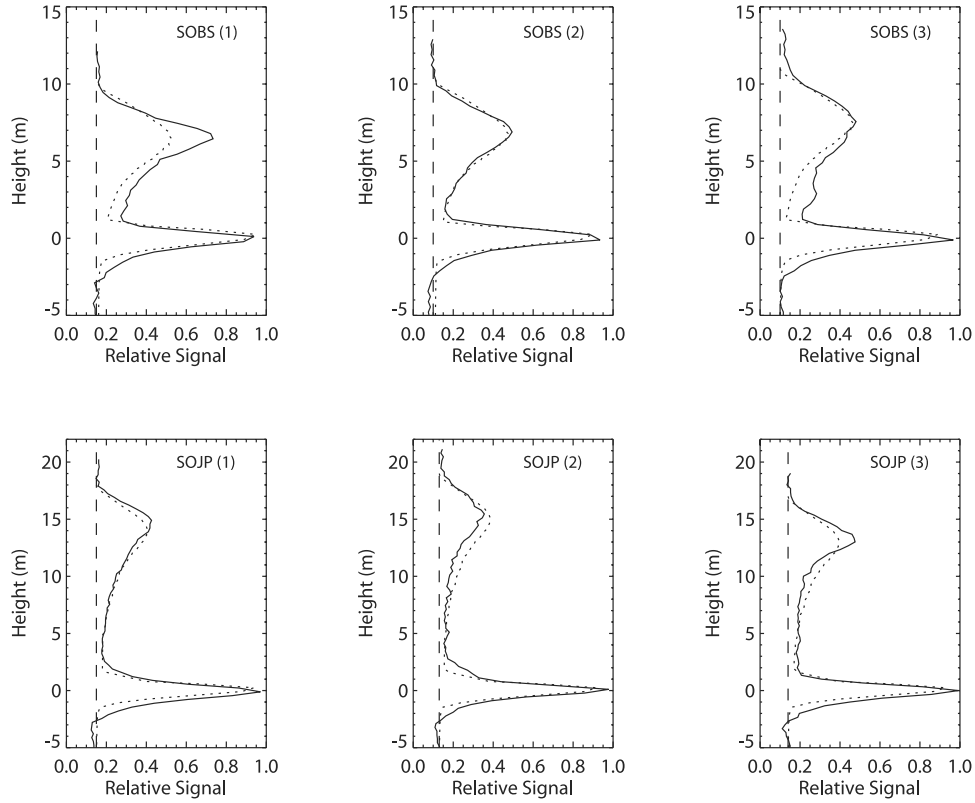

Figure 5a. SLICER waveforms and model simulations for SOBS and SOJP study sites of BOREAS. The solid curves represent the SLICER signals. The dotted curves are the simulated waveforms. The noise level is shown as a vertical dashed line.

story, in the second and third mature and intermediate plots, is acceptable. The majority of radiation is intercepted in the upper layer of the canopy in view of high foliage density in these stands.

6. Contribution of Multiple Scattering

[51] The simulated returns generated from single and multiple scattering are next compared to evaluate the contribution of multiply scattered photons. From the plots shown in Figures 5a and 5b, those that agreed best with SLICER data were chosen for this investigation; one plot for each forest stand. These are SOBS (2), SOJP (1), mature (3), and intermediate (1). The model-simulated signals originating from single scattering were added to each plot. The results are shown in Figure 6.

[52] The inclusion of multiple scattering magnifies the signal and enhances significantly the lower part of the waveform. In general, multiply scattered photons carry information on canopy structural parameters, namely, foliage density (defined in equation (3)) and gap fraction. When a photon path in the canopy is limited to a single interaction, the total travel time is the round trip time between the sensor and the interaction point: $t_{total} = t_{ps}$. If a photon has interacted several times before leaving the canopy in the direction of the sensor, the total travel time is increased to $t_{total} = t_{ps} + t_{pm}$, where t_{pm} is the extra time due to multiple scattering. This extra time depends on two variables: the number of interactions and the mean distance of photon travel between two interactions (photon mean free path). The photon mean free path is inversely proportional to the extinction coefficient $\sigma(\vec{r}, \vec{\Omega})$, which is directly related to canopy structure. A vegetation canopy with high density will generate more multiple scattering but with relatively short free paths. Conversely, in sparse canopies, the contribution of multiple scattering will be relatively lower but with longer paths.

[53] In case of sparse canopies, single scattering approximation models are expected to provide good simulations of lidar recorded signals. A hybrid geometric optical and radiative transfer model (GORT) proposed by *Ni-Meister et al.* [2001], was tested with data from four BOREAS sites: SOBS, SOJP, NOBS (northern old black spruce), and NOJP (northern old jack pine). Selected SLICER waveforms were normalized by the maximum signal (ground return). The model provided good agreement between the measured and simulated waveforms, but the relative amplitude of vegetation return was low: less than 0.15 for the SOBS site and less than 0.1 for the others. This indicates that the density of measured vegetation was relatively low and the effects of multiple scattering were probably insignificant. For the study presented here, the lower boundary of relative amplitude was 0.3 for SOJP and 0.4 for SOBS.

[54] The waveform shapes change dramatically in a set of measurements for the same site. It depends on the density of vegetation and the number of trees within the footprint. As a result, some waveforms may show effects of multiple scattering, while the others may not. The effect of multiple

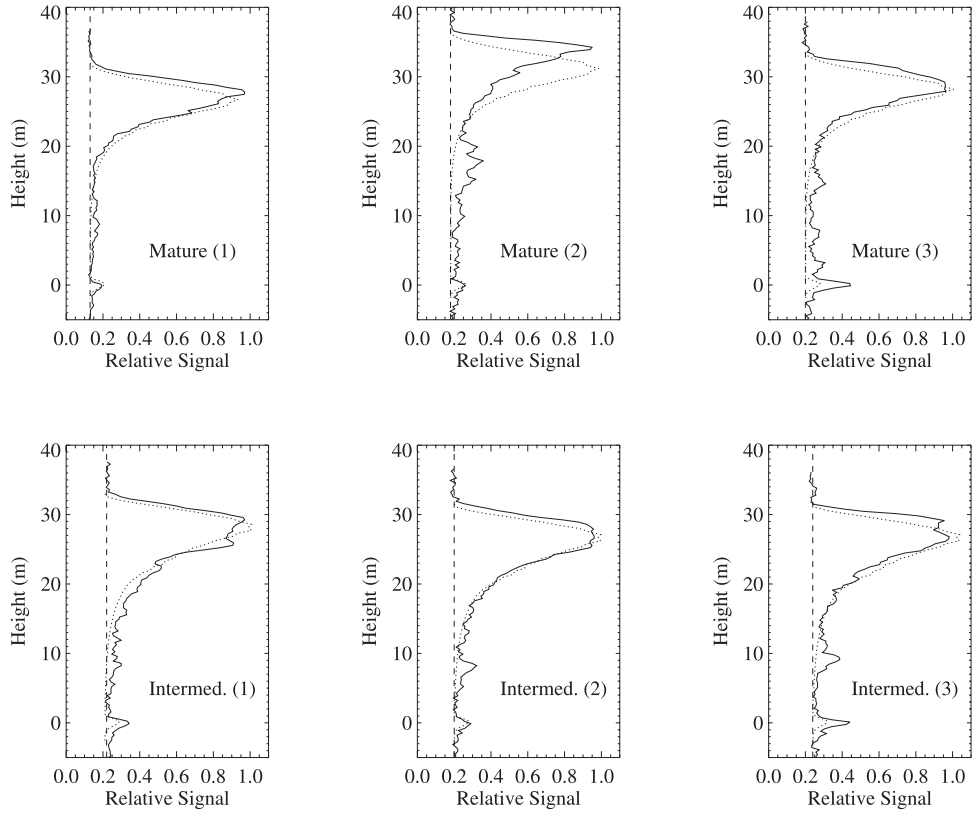

Figure 5b. SLICER waveforms and model simulations for SERC mature and intermediate forest stands. The solid curves represent the SLICER signals. The dotted curves are the simulated waveforms. The noise level is shown as a vertical dashed line.

scattering also depends on the amplitude and duration of a laser pulse. The model shows that this effect is more significant in the simulations with longer pulse widths. An increase of the amplitude makes it more detectable.

7. Conclusions

[55] A new model for simulating the propagation of lidar signals through vegetation canopies useful in studies on remote sensing of forest structure is presented in this paper. The model is based on the numerical solution of a time-dependent stochastic radiative transfer equation. Such an approach includes multiple scattering which leads to a better approximation of lidar returns.

[56] Model simulations are compared with SLICER signals from four forest sites to evaluate the model performance. The sites include two coniferous forest stands in BOREAS southern study areas, old jack pine and old black spruce, and two broadleaf forest stands in eastern Maryland, of different age and structure, with overstory dominated by tulip poplar. The model was parameterized with tree structural parameters available from field campaigns conducted at these sites. The overall agreement between the model simulations and the recorded signals is good. For both coniferous and deciduous stands, multiple scattering not only leads to a slower decay of the waveform, but also magnifies the return signal. The difference between the return signals generated from single and multiple scattering may result in a physically based algorithm for retrieval of tree structural parameters.

[57] The chief limitation of the model is characterizing the probability functions, p(z) and K(z, ξ, $\vec{\Omega}$), which quantify the canopy structure. However, in the absence of correlation between vegetated elements in different planes, only modeling of horizontal density of vegetation is required. Further improvement in model performance can be achieved by more accurate modeling of p(z) and K(z, ξ, $\vec{\Omega}$).

[58] Perhaps most significantly, the model will facilitate studies that relate canopy vertical and spatial structures to lidar waveforms. By better understanding the effects of stem density, canopy roughness, canopy layering, leaf distribution, and so forth, on the resulting waveforms, we should gain insight into how such data may then best be used to estimate important land surface variables, such as biomass.

Appendix A: Discrete Schemes of the Equations for U ($\vec{r}$, z, $\vec{\Omega}$)

[59] In the general form, equations (22) and (26) are written as

$$U\left(t_i, z, \vec{\Omega}\right) + \frac{\sigma\left(\vec{\Omega}\right)}{\left|\mu\left(\vec{\Omega}\right)\right|} \int_0^z K\left(z, \xi, \vec{\Omega}\right) \cdot U\left(t_i, \xi, \vec{\Omega}\right) d\xi$$

$$= F\left(t_i, z, \vec{\Omega}\right) + G\left(t_{i-1}, z, \vec{\Omega}\right). \quad \text{(A1)}$$

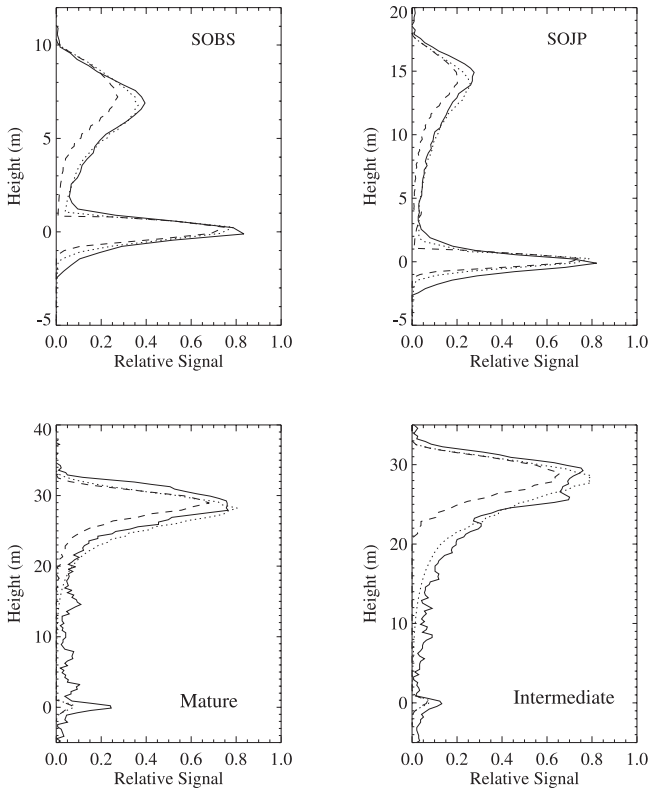

Figure 6. SLICER waveforms and model simulations with and without multiple scattering for four different sites. The solid curves represent the SLICER signals. The single scattering simulations are shown with dashed curves, while the dotted curves represent multiple scattering simulations. Noise is subtracted.

To solve equation (A1), the following dicretization scheme is used:

$$U\left(t,k,\vec{\Omega}\right)+\frac{\sigma\left(\vec{\Omega}\right)}{\left|\mu\left(\vec{\Omega}\right)\right|}\sum_{j=1}^{j=k}W_{k,j}\cdot K\left(k,j,\vec{\Omega}\right)\cdot U\left(t,j,\vec{\Omega}\right)=F\left(t,k,\vec{\Omega}\right)+G\left(t-1,k,\vec{\Omega}\right),\quad(A2)$$

where $W_{k,j}$ is a weight, which depends on the scheme used for approximation of the integrals. Equation (A2) can be rewritten in an equivalent form:

$$U\left(t,k,\vec{\Omega}\right)+\frac{\sigma\left(\vec{\Omega}\right)}{\left|\mu\left(\vec{\Omega}\right)\right|}\cdot W_{k,k}\cdot K\left(k,k,\vec{\Omega}\right)\cdot U\left(t,k,\vec{\Omega}\right)=F\left(t,k,\vec{\Omega}\right)-\frac{\sigma\left(\vec{\Omega}\right)}{\left|\mu\left(\vec{\Omega}\right)\right|}\cdot\sum_{j=1}^{j=k-1}W_{k,j}\cdot K\left(k,j,\vec{\Omega}\right)\cdot U\left(t,j,\vec{\Omega}\right)+G\left(t-1,k,\vec{\Omega}\right).\quad(A3)$$

Solving equation (A3) for U(t, k, $\vec{\Omega}$) results in:

$$U\left(t,k,\vec{\Omega}\right)=\frac{F\left(t,k,\vec{\Omega}\right)-\frac{\sigma\left(\vec{\Omega}\right)}{\left|\mu\left(\vec{\Omega}\right)\right|}\cdot\sum_{j=1}^{j=k-1}W_{k,j}\cdot K\left(k,j,\vec{\Omega}\right)\cdot U\left(t,j,\vec{\Omega}\right)+G\left(t-1,k,\vec{\Omega}\right)}{1+\frac{\sigma\left(\vec{\Omega}\right)}{\left|\mu\left(\vec{\Omega}\right)\right|}\cdot W_{k,k}\cdot K\left(k,k,\vec{\Omega}\right)}\quad(A4)$$

Here $\vec{\Omega}$ is a parameter of the equation. Function U(t, k, $\vec{\Omega}$) depends on G(t − 1, k, $\vec{\Omega}$), which, in turn, depends on the values of the mean intensity, estimated at the previous time step (t − 1). Initial values of U(t, k, $\vec{\Omega}$), when k = 1 or t = 1, are specified in the boundary conditions (see equation (5)).

Notation

Roman alphabet

$E_n(t)$	total amount of radiant energy of photons scattered n times (W m^{-2}).
$f_\lambda(t)$	intensity of a transmitted pulse (W $m^{-2} \cdot sr^{-1}$).
$G(\vec{r},\vec{\Omega})$	mean projection of leaf normals in direction $\vec{\Omega}$.
H	canopy height (m).
$I(t,\vec{r},\vec{\Omega})$	radiance at spatial point $\vec{r}$ in direction $\vec{\Omega}$ at time t (W · m^{-2} · sr^{-1}).
$\bar{I}\left(t,z,\vec{\Omega}\right)$	mean radiance, averaged over horizontal plane z (W · m^{-2} · sr^{-1}).
$K(z,\xi,\vec{\Omega})$	correlation function of foliage elements located in horizontal planes z and along direction $\vec{\Omega}$.
L	crown length (m).
p(z)	probability to find a foliage element at depth z.
S_z	horizontal plane at depth z.
$U(t,z,\vec{\Omega})$	mean radiance, averaged over the vegetated portion of horizontal plane z (W · m^{-2} · sr^{-1}).
$u_L(\vec{r})$	foliage area volume density (m^{-1}).

Greek alphabet

$\chi(\vec{r})$	indicator function.
$\delta(\vec{\Omega}-\vec{\Omega}_0)$	Dirac delta function in direction space.
$\frac{1}{\pi}\Gamma(\vec{r},\vec{\Omega}'\rightarrow\vec{\Omega})$	area scattering phase function (sr^{-1}).
λ	wavelength (nm).
$\mu(\vec{\Omega})$	cosine of the polar angle of direction $\vec{\Omega}$.
$\rho_L(\lambda)$	leaf hemispherical reflectance.
ρ^n	conditional probability for a photon to be scattered n times.
$\rho_{soil}(\lambda)$	soil hemispherical reflectance.
$\sigma(\vec{\Omega})$	extinction coefficient (m^{-1}).
$\sigma_S(\vec{\Omega}'\rightarrow\vec{\Omega})$	differential scattering coefficient ($m^{-1} \cdot sr^{-1}$).
$\tau_L(\lambda)$	leaf hemispherical transmittance.
$\vec{\Omega}=\{\Omega_u,\Omega_y,\Omega_z\}$	unit vector of a solid angle.
$\vec{\Omega}_0$	direction of a transmitted pulse.

[60] **Acknowledgments.** The authors would like to thank David Harding and Kathy Still for providing the SLICER data. They would also like to thank the anonymous reviewers for helpful comments. This work was supported by NASA Headquarters under the Earth System Science Fellowship grant NGT5-30462.

References

Blair, J. B., and M. A. Hofton, Modeling laser altimeter return waveforms over complex vegetation using high-resolution elevation data, *Geophys. Res. Lett.*, *26*, 2509–2512, 1999.

Castel, T., A. Beaudoin, N. Floury, T. Le Toan, Y. Caraglio, and J. F. Barczi, Deriving forest canopy parameters for backscatter models using the AMAP architectural plant model, *IEEE Trans. Geosci. Remote Sens.*, *39*(3), 571–583, 2001.

Chen, J. M., P. M. Rich, S. T. Gower, J. M. Norman, and S. Plummer, Leaf area index of boreal forests: Theory, techniques, and measurements, *J. Geophys. Res.*, *102*, 29,429–29,443, 1997.

Chen, J. M., J. Liu, J. Cihlar, and M. L. Goulden, Daily canopy photosynthesis model through temporal and spatial scaling for remote sensing applications, *Ecol. Modell.*, *124*, 99–119, 1999.

Davis, A. B., R. F. Cahalan, J. D. Spinhirne, M. J. McGill, and S. P. Love, Off-beam lidar: An emerging technique in cloud remote sensing based on radiative green-function theory in the diffusion domain, *Phys. Chem. Earth, Part B*, *24*(6), 757–765, 1999.

Davis, A. B., D. M. Winker, and M. A. Vaughan, First retrievals of dense cloud properties from off-beam/multiple-scattering lidar data collected in space, in *Laser Remote Sensing of the Atmosphere: Selected Papers from the 20th International Conference on Laser Radar*, edited by A. Dabas and J. Pelon, pp. 35–38, École Polytech., Palaiseau, France, 2001.

Drake, J. B., R. Dubayah, D. B. Clark, R. G. Knox, J. B. Blair, M. A. Hofton, R. L. Chazdon, J. F. Weishampel, and S. Prince, Estimation of tropical forest structural characteristics using large-footprint lidar, *Remote Sens. Environ.*, *79*, 305–319, 2002.

Drake, J. B., R. Dubayah, R. G. Knox, D. B. Clark, and J. B. Blair, Sensitivity of large-footprint lidar to canopy structure and biomass in a neotropical forest, *Remote Sens. Environ.*, *81*, 378–392, 2002.

Dubayah, R., J. B. Blair, J. Bufton, D. Clark, J. JaJa, R. Knox, S. Luthcke, S. Prince, and J. Weishampel, The vegetation canopy lidar mission, in *Land Satellite Information in the Next Decade II: Sources and Applications*, pp. 100–112, Am. Soc. for Photogramm. and Remote Sens., Bethesda, Md., 1997.

Dubayah, R., R. Knox, M. Hofton, J. B. Blair, and J. Drake, Land surface characterization using lidar remote sensing, in *Spatial Information for Land Use Management*, edited by M. Hill and R. Aspinall, Gordon and Breach, Newark, N. J., 2000.

Germogenova, T. A., *The Local Properties of the Solution of the Transport Equation* (in Russian), Nauka, Moscow, 1986.

Govaerts, Y. M., *A Model of Light Scattering in Three-Dimensional Plant Canopies: A Monte Carlo Ray Tracing Approach*, 186 pp., Space Appl. Inst., Joint Res. Cent., Eur. Comm., Luxembourg, 1996.

Harding, D. J., J. B. Blair, D. L. Rabine, and K. L. Still, SLICER airborne laser altimeter characterization of canopy structure and sub-canopy topography for the BOREAS northern and southern study regions: Instrument and data product description, in *Technical Report Series on the Boreal Ecosystem-Atmosphere Study (BOREAS)*, vol. 93, edited by F. G. Hall and J. Nickeson, *NASA Tech. Memo., TM-2000-20,9891*, 45 pp., 2000.

Harding, D. J., M. A. Lefsky, G. G. Parker, and J. B. Blair, Laser altimeter canopy height profiles: Methods and validation for closed-canopy, broadleaf forests, *Remote Sens. Environ.*, *76*, 283–297, 2001.

Knyazikhin, Y., J. Kranigh, R. B. Myneni, O. Panfyorov, and G. Gravenhorst, Influence of small-scale structure on radiative transfer and photosynthesis in vegetation cover, *J. Geophys. Res.*, *103*, 6133–6144, 1998.

Lefsky, M. A., D. Harding, W. B. Cohen, G. Parker, and H. H. Shugart, Surface lidar remote sensing of basal area and biomass in deciduous forests of eastern Maryland, USA, *Remote Sens. Environ.*, *67*, 83–98, 1999a.

Lefsky, M. A., W. B. Cohen, S. A. Acker, G. G. Parker, T. A. Spies, and D. Harding, Lidar remote sensing of the canopy structure and biophysical properties of Douglas-fir western hemlock forests, *Remote Sens. Environ.*, *70*, 339–361, 1999b.

Lefsky, M. A., W. B. Cohen, S. A. Acker, G. G. Parker, and D. J. Harding, Lidar remote sensing for ecosystem studies, *BioScience*, *52*(1), 19–30, 2002.

Malvagi, F., R. N. Byrne, G. C. Pomraning, and R. C. J. Somerville, Stochastic radiative transfer in a partially cloudy atmosphere, *J. Atmos. Sci.*, *50*, 2146–2158, 1993.

Means, J. E., S. A. Acker, D. J. Harding, J. B. Blair, M. A. Lefsky, W. B. Cohen, M. E. Harmon, and W. A. McKee, Use of large-footprint scanning airborne lidar to estimate forest stand characteristics in the western cascades of Oregon, *Remote Sens. Environ.*, *67*, 298–308, 1999.

Middleton, E. M., S. S. Chan, R. J. Rusin, and S. K. Mitchell, Optical properties of black spruce and jack pine needles at BOREAS sites in Saskatchewan, Canada, *Can. J. Remote Sens.*, *23*(2), 108–119, 1997.

Myneni, R. B., Modeling radiative transfer and photosynthesis in three-dimensional vegetation canopies, *Agric. For. Meteorol.*, *55*, 323–344, 1991.

Ni-Meister, W., D. L. B. Jupp, and R. Dubayah, Modeling lidar waveforms in heterogeneous and discrete canopies, *IEEE Trans. Geosci. Remote Sens.*, *39*(9), 1943–1958, 2001.

Oliver, C. D., and B. C. Larson, *Forest Stand Dynamics*, McGraw-Hill, New York, 1990.

Parker, G. G., M. A. Lefsky, and D. J. Harding, Light transmittance in forest canopies determined using airborne laser altimetry and in-canopy quantum measurements, *Remote Sens. Environ.*, *73*, 298–310, 2001.

Ranson, K. J., G. Sun, J. F. Weishampel, and R. G. Knox, Forest biomass from combined ecosystem and radar backscatter modeling, *Remote Sens. Environ.*, *59*, 118–133, 1997.

Ross, J., *The Radiation Regime and Architecture of Plant Stands*, Dr. W. Junk, Norwell, Mass., 1981.

Shabanov, N. V., Y. Knyazikhin, F. Baret, and R. B. Myneni, Stochastic modeling of radiation regime in discontinuous vegetation canopies, *Remote Sens. Environ.*, *74*, 125–144, 2000.

Shultis, J. K., and R. B. Myneni, Radiative transfer in vegetation canopies with an isotropic scattering, *J. Quant. Spectrosc. Radiat. Transfer*, *39*, 115–129, 1988.

Sun, G., and K. J. Ranson, Modeling lidar returns from forest canopies, *IEEE Trans. Geosci. Remote Sens.*, *38*(6), 2617–2626, 2000.

Titov, G. A., Statistical description of radiation transfer in clouds, *J. Atmos. Sci.*, *47*(1), 24–38, 1990.

Vainikko, G. M., The equation of mean radiance in broken cloudiness (in Russian), *Tr. Mosk. Gos. Kom. SSSR Meteorol. Invest.*, *21*, 28–37, 1973a.

Vainikko, G. M., Transfer approach to the mean intensity of radiation in noncontinuous clouds (in Russian), *Tr. Mosk. Gos. Kom. SSSR Meteorol. Invest.*, *21*, 38–57, 1973b.

A. B. Davis, Space and Remote Sensing Sciences Group, Los Alamos National Laboratory, Los Alamos, NM 87545, USA.

R. Dubayah, Department of Geography, University of Maryland, College Park, MD 20742, USA.

Y. Knyazikhin, S. Y. Kotchenova, R. B. Myneni, and N. V. Shabanov, Department of Geography, Boston University, 675 Commonwealth Avenue, 457, Boston, MA 02215, USA. (skotchen@bu.edu)